Midspatial-frequency Surface Errors

Mike Lampton,UCB SSL

April 7, 2014

1 Introduction

A key factor in any fiber-fed spectroscopy measurement is the fraction of target light that enters the fiber. For faint astronomical targets – well below the sky continuum background – the fiber must not only capture some of the target light but also reject the unwanted night sky. The optimum fiber size is roughly the 50% encircled energy size of the target. QSOs are expected to fall a bit higher than 50% and galaxies a bit lower.

Detailed studies of the statistical distribution of emission-line galaxy sizes and the May-all/MOSAIC delivered image quality have been released (see DocDB-392v1 (2013) and references therein). Those convolutions predict a median capture fraction = 43% of the galaxy light onto a 1.46 arcsecond diameter fiber core. This model would be appropriate if galaxy light were gathered by the MOSAIC prime focus corrector (Jacoby et al 1998) onto an ideally centered photometry aperture. The published DIQ star-image distributions (Dey and Valdes 2014) include seeing, the optical performance of the MOSAIC corrector, short-term telescope guiding, focus, and pixellization.

The DESI system throughput budget includes median galaxy PSF effects onto the fiber. This budget spreadsheet, DocDB-347v3, starts with the above modelled PSF and modifies it in five ways:

- The MOSAIC design residual aberrations are modelled and subtracted (row 19);
- The Echo-22 design residual aberrations are modelled and added (row 25);
- The astrometric target location errors are modelled and added (row 29);
- The guider absolute position errors are estimated and added (rows 37,38);
- The fiber positioner location errors are estimated and added (rows 39-41).

This modelling predicts a net median fiber throughput of 42% on median-size ELGs with median seeing, and gives a curve showing the throughput cost of small amounts of added Gaussian blur.

In this document, I will estimate the sensitivity of the corrector blur to mid-spatial frequency lens finishing errors. DESI is unlikely to be worse than the corresponding errors in the MOSAIC camera, whose PSF is already built into our model. However this calculation evaluates the system throughput sensitivity to such errors, and may therefore help inform the upcoming discussions on cost/benefit for the corrector lens finishing and testing process.

Also I include a short section about the consequences of MSF corrector errors on the fiber view camera's centroid error budget.

2 Power Spectral Density

Optical surface deviations occur spanning many length scales and with a continuum of amplitudes. The statistical description of these deviations is customarily quantified using the power spectral density, PSD(f), which gives the surface variance dz^2_{rms} contributed by each narrow group of spatial frequencies df. In the azimuthally averaged two dimensional PSD formulism, those 2D components are parameterized by a spatial frequency magnitude f that represents an annular zone in frequency space whose area is the annulus area $dA = 2\pi f df$. (There is an analogous one dimensional PSD that has been integrated, not just averaged, over azimuth; it is defined as $PSD_{2dim} \cdot 2\pi f$.) The 2D PSD functions have units of $length^4$. To avoid the gnarly interplay of various powers of μm (wavelengths), nm (surface height errors), and m or mm (optic diameters) to be developed below, I will adopt all lengths in m, spatial frequencies in cycles/m, all angles in radians, and therefore PSD units of m^4.

I assume the surface errors are small-amplitude but large-wavelength compared to the optical wavelengths in use, so that the surface slopes are $\ll 1$ radian. The net surface variance z^2_{rms} in a given band of spatial frequencies a, b is an integral of the PSD. The net slope variance s^2_{rms} is another integral of the PSD that includes an extra factor of $4\pi^2 f^2$ to account for the spatial derivative. Slope variance has become an important optical specification (Rogers 2007) and I review here how it controls MSF blur. Over any frequency band a, b of interest:

$$z^2_{rms} = \int_a^b dz^2_{rms} = \int_a^b 2\pi f df PSD(f) \tag{1}$$

$$s^2_{rms} = \int_a^b ds^2_{rms} = \int_a^b 8\pi^3 f^3 df PSD(f) \tag{2}$$

3 Three Spatial Frequency Bands

Imperfections in optical surfaces are customarily divided into three bands demarcated by three spatial frequencies f_A, f_B, f_C:

- LSFs, $f_A < f < f_B$;
- MSFs, $f_B < f < f_C$;
- HSFs, $f_C < f < \infty$.

This distinction is largely driven by modeling methods, test methods, and consequences for optical image quality and throughput. At LSFs, the surface profile is easily measured by interferometry and modelled by Zernike coefficients 4-36, and is thought of as figure error, associated with the Seidel aberrations. Traditionally the bottom Zernike coefficients that describe piston, tilt, and power are not part of the LSF specification because they can be

elimininated by alignment and focus. To span the 4-36 Zernike range, the LSF spatial frequency bounds are determined by the lens diameter D_{lens} and are commonly taken to be $f_A = 1$ cycle$/D_{lens}$ and $f_B = 4$ cycles$/D_{lens}$. The MSF realm extends upward from f_B to a higher frequency f_C where the HSFs begin. At HSFs, the surface is modelled as a scatterer that removes light from the spot radius of interest and therefore it does not broaden the point spread function (PSF) but instead attenuates it. So, this third crossover frequency f_C depends on the application.

3.1 Objective lens at pupil

This distinction can be made quantitative using the first-order diffraction model (see below) and results in $f_C = \theta_{interest}/\lambda$ where $\theta_{interest}$ is the angular radius of the PSF patch on the sky and λ is the light's wavelength. For a full-aperture-pupil optic, the diffraction-limited angular spot radius is $\theta_{pupil} \simeq \lambda/D_{pupil}$. If $\theta_{interest} \simeq 4\theta_{pupil}$, then $f_C \simeq f_B$ and the MSF band collapses to nothing. However many applications must control light well beyond the pupil diffraction pattern and therefore have $\theta_{interest} \gg 4\theta_{pupil}$. Such applications (e.g. planet searches near stars) call for MSF band specifications.

3.2 Corrector lenses in converging light

Each DESI corrector lens surface differs in two important ways from the simple objective pupil case. First, there are now three diameters at work, not just one: $D_{beam} < D_{lens} < D_{pupil}$ as illustrated in the cartoon below. Owing to the brightness theorem, any sky angle θ_{sky} becomes magnified by a factor M at a surface with a smaller beam diameter, giving $\theta_{lens}/\theta_{sky} = M = D_{pupil}/D_{beam}$. Second, the dividing line between MSFs (where scattering enlarges the PSF) and HSFs (where light is simply lost) is the fiber radius on the sky θ_{fiber}. Accordingly I replace $\theta_{interest}$ by θ_{fiber}, and obtain $f_C = M\theta_{fiber}/\lambda$. These two changes raise the HSF base f_C to a value higher than f_B, opening up the MSF band.

For each DESI corrector lens surface, I adopt these boundary frequency and sky angle formulas, and show one numerical example with D_{lens}=1m, $\lambda = 1\mu m$ and $M = 4$.

Table 1: Spatial Frequency Bands and Corresponding Sky Angles

	frequency	θ_{sky}	Example freq	Example θ_{sky}
f_A	$1/D_{lens}$	λ/MD_{lens}	1 cycle/m	0.25 μrad
f_B	$4/D_{lens}$	$4\lambda/MD_{lens}$	4 cycle/m	1.0 μrad
f_C	$M\theta_{fiber}/\lambda$	θ_{fiber}	14 cycles/m	3.5 μrad

4 Diffracted Energy

The deviation of refracted light from its nominal Snell's law direction is governed by diffraction. Each sinusoidal ripple component of surface irregularity modifies the wavefront's phase. At near normal incidence, the phase errors and the surface errors are related to each other via the optical wavelength λ and the refractive index N of the material:

$$\phi_{rms} = \frac{2\pi}{\lambda} \cdot (N-1) \cdot z_{rms} \tag{3}$$

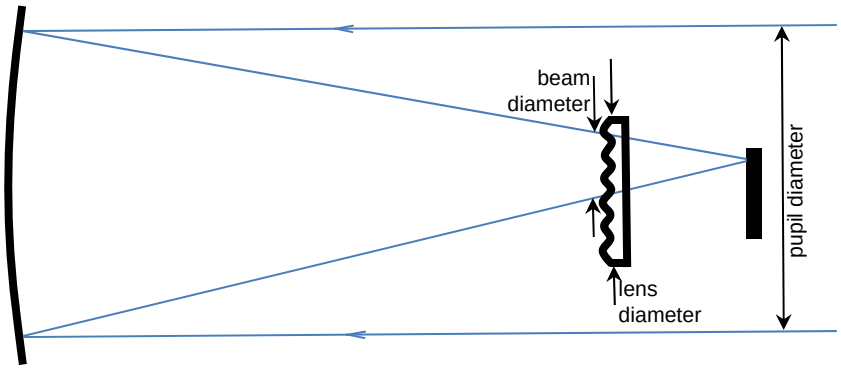

Figure 1: Cartoon illustrating an irregular corrector lens surface. Its working beam diameter is smaller than the telescope pupil, so that, by the brightness theorem, angles at each lens surface are magnified by a factor D_{pupil}/D_{beam} compared to their size on the sky. Equivalently, a deviation angle introduced at the lens surface is demagnified by that same factor when converted to an angle on the sky. After Tamkin et al 2010 figure 3.

From the theory of sinusoidal phase gratings (section 9 below), the fraction of light diffracted into order n depends on the amplitude of the sinusoidal wavefront ϕ_{peak} via the Bessel function J_n:

$$\eta = 2J_n^2(\phi_{peak}) = 2J_n^2(\sqrt{2}\phi_{rms}) \tag{4}$$

Here I am interested in low amplitude ripples ($\phi \ll 1$). In this case only the zero order and first order diffractions are important. Zero order corresponds to no ray deviation and represents the undisturbed wavefront; it has nearly unit intensity. First order describes the PSF broadening. In this limit, $J_1^2(x) \to x^2/4$ and:

$$\eta = \frac{4\pi^2(N-1)^2}{\lambda^2} \cdot z_{rms}^2 \tag{5}$$

This relationship shows that within any given band, the fraction of light that is diffracted is simply proportional to the mean square surface deviation over the wavefront. For $z_{rms} = 0.1$ waves, about 10% of the light is diffracted while the rest remains in the zero order image.

It is useful at this point to decompose the total scattering η into its contributions from each spatial frequency band $f, f+df$. This decomposition follows exactly the decomposition of z_{rms}^2 in equation 1, and gives

$$d\eta = \frac{8\pi^3(N-1)^2}{\lambda^2} f df PSD(f) \tag{6}$$

With this decomposition, it is now straightforward to assess the amount of diffracted light sent into each angle. From diffraction grating theory, the deviation in ray direction caused by a periodic component at spatial frequency f and integer order of diffraction n is:

$$\theta_{local} = n \cdot f \cdot \lambda \tag{7}$$

This local (at lens) deviation angle can be expressed as a sky angle by dividing it by the magnification $M = D_{pupil}/D_{beam}$ appropriate for the beam size at that surface.

At this point we can model any given sinusoidal PSD component to determine where its light falls with respect to the undiffracted center, and its intensity compared to the undiffracted incoming beam. Using the statistical PSD description, the first order contribution to the angular scattering variance from the elementary frequency group $f, f + df$ is

$$d\theta^2_{local} = \theta^2 d\eta = 8\pi^3(N-1)^2 \cdot f^3 df \cdot PSD(f) \tag{8}$$

which may be recast as θ^2_{sky} by dividing it by M^2.

The expression $8\pi^3 f^3 df PSD(f)$ will be familiar from equation 2: it is the mean square slope contribution from the spatial frequency group $f, f+df$. So, whatever the PSD function might be, and whatever band of spatial frequencies you may choose, the angular blur on the sky is directly related to the rms slope (they are both angles, so this should not be surprising) by

$$d\theta_{sky,rms} = \frac{N-1}{M}\, ds_{rms} \tag{9}$$

For example, one μrad of slope error in a given spatial frequency band causes about 0.5 μrad (0.1 arcsecond) of local rms blur from that same band, which on the sky reduced by a factor of 4 when M=4, giving 0.025 arcsecond rms.

5 Power Law PSDs

The single most common model for MSF surfaces is the power law PSD (see references below) whose exponent p is usually found to range from 1 to 4:

$$PSD(f) = Af^{-p} \tag{10}$$

Integrating this over any finite band a, b we have[1]

$$z^2_{rms} = \frac{2\pi A}{2-p}[b^{2-p} - a^{2-p}] \tag{11}$$

$$s^2_{rms} = \frac{8\pi^3 A}{4-p}[b^{4-p} - a^{4-p}] \tag{12}$$

$$\tag{13}$$

These equations may of course be reversed to give the A coefficient that will yield the maximum allowable surface error, or slope error, or diffracted light, or added angular variance for any band and given power law index. Figure 2 below shows some power law PSDs with given z_{rms} and s_{rms} values. In this figure, the (f_A, f_B, f_C) trio are from the example in Table 1 above.

Next I will apply the foregoing material to the twelve DESI corrector surfaces listed in Figure 3 below. Each surface has its own lens diameter and beam diameter, obtained

[1]When you need it, $\lim_{q\to 0}\,(b^q - a^q)/q = ln(b/a)$.

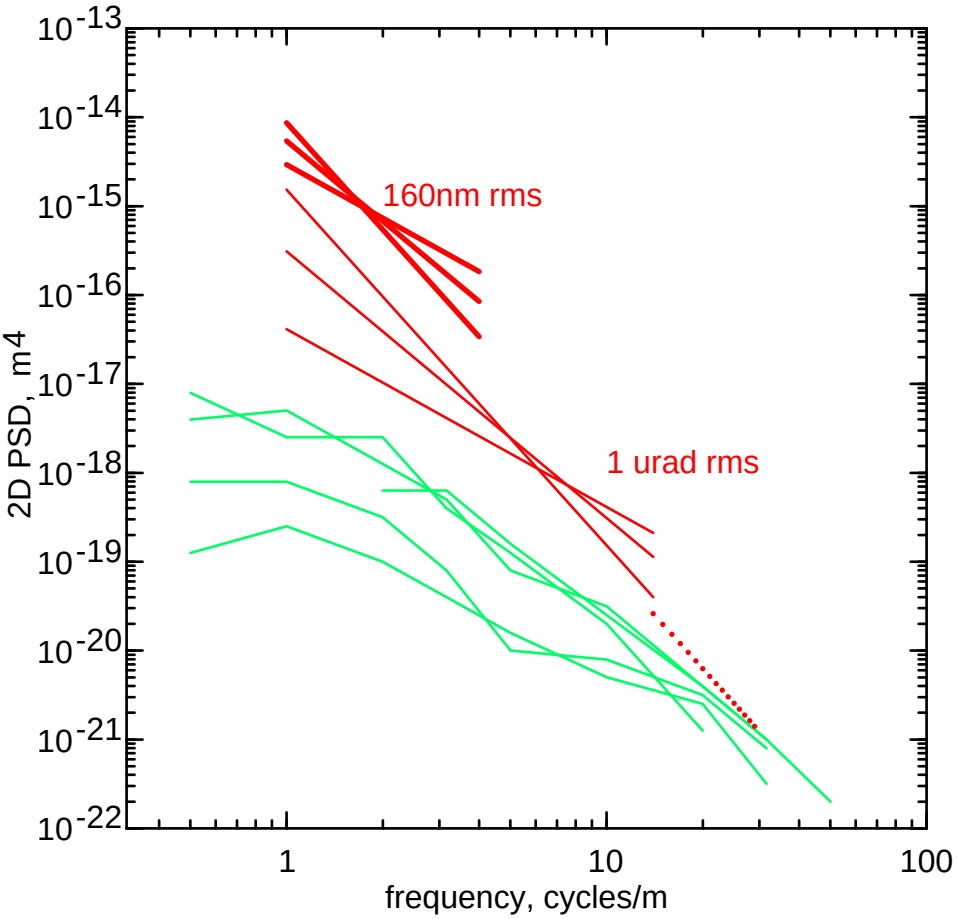

Figure 2: Red: DESI corrector surface C1front specification from DocDB 602v2 Table 1 page 5, plotted as various PSD power laws. Heavy lines: LSF region, 1 wave P-V at 633nm or 160nm RMS, for assumed power law index 2, 3, and 4. Light lines: 1 μrad RMS slope in the combined LSF+MSF bands, same indices. Dotted line: example of an HSF spec with $p = 4$ and $A = 10^{-15}$. Green: for comparison, five high quality mirror surface measured PSDs are plotted, taken from Cohen and Hull (2004) figures 3, 7, and 11.

from DESI DocDB 329 Table I and a follow-on report "Slope Errors" (M. Sholl 14 Feb 2014). These broadband slope tolerances directly drive the angular blur contribution of each surface, which is shown in Column 6. For reference I also show the triplet of spatial frequencies associated with each surface, as derived above.

Surface	Lens Diam m (note 1)	BeamDiam m (note 2)	Sky Magnif	Slope Spec µrad (note 2)	Estimated rmsBlur, µrad	fA cycles/m	fB cycles/m	fC cycles/m	loss above fC
C1front	1.140	0.690	5.65	1	0.081	0.88	3.51	24.7	6.7E-05
C1back	1.140	0.644	6.06	1	0.076	0.88	3.51	26.5	5.8E-05
C2front (asph)	0.850	0.390	10.00	5	0.230	1.18	4.71	43.8	2.1E-05
C2back	0.850	0.363	10.74	2	0.086	1.18	4.71	47.0	1.9E-05
A1front	0.800	0.316	12.34	2	0.075	1.25	5.00	54.0	1.4E-05
A1back	0.800	0.302	12.91	2	0.071	1.25	5.00	56.5	1.3E-05
A2front	0.804	0.296	13.18	2	0.070	1.24	4.98	57.6	1.2E-05
A2back	0.804	0.286	13.64	2	0.067	1.24	4.98	59.7	1.2E-05
C3front (asph)	0.834	0.256	15.23	5	0.151	1.20	4.80	66.7	9.2E-06
C3back	0.834	0.254	15.35	2	0.060	1.20	4.80	67.2	9.1E-06
C4front	1.034	0.148	26.35	3	0.052	0.97	3.87	115.3	3.1E-06
C4back	1.034	0.111	35.14	3	0.039	0.97	3.87	153.7	1.7E-06
				total RSS blur, µrad=	0.351			Total loss=	2.4E-04

(1) from DocDB 329 Table 1, Echo22 Prescription
(2) from Sholl "Slope Errors" 14 Feb 2014 chart 4

Figure 3: This spreadsheet lists the lens and beam diameters for each of the twelve refracting surfaces of Echo22. From those I calculate the sky magnification, and from the allowed slope error I calculate an estimate of the sky blur contribution, whose RSS sum is shown at the bottom. For reference I also calculate the triplet of spatial frequencies f_A, f_B, f_C discussed in the text. The f_C value depends on wavelength and fiber radius, for which I adopt 0.8 μm and 3.5 μradian. Losses at high spatial frequencies, above f_C, are discussed in section 6.2 below.

6 Two Throughput Effects

For DESI we feed fibers and want to minimize our optical throughput losses. There are two contributors revealed in this analysis, distinguished by spatial frequencies below and above the fiber-determined cutoff frequency f_C. At lower frequencies, the image grows slightly and some of the galaxy image is pushed outside the fiber, while at higher frequencies the diffracted light is sent into the wings beyond the fiber and is lost.

6.1 Light Loss due to Image Growth

Our DESI image profiles have many contributors. Following DESI-doc-347, I concentrate on a Moffat profile whose β=3.5 and FWHM=1.3 arcsecond, whose core radius is then 1.4 arcseconds or 6.8 μradian.[2] With $x \equiv r/r_{core}$, a Moffat profile encircled energy and its derivative is given by

$$EE(x) = 1 - (1 + x^2)^{1-\beta} \tag{14}$$

$$dEE/dx = (2\beta - 2)x(1 + x^2)^{-\beta} \tag{15}$$

$EE(x)$ is plotted in Figure 4 below. The vertical line is located at the fiber radius, 0.73 arcseconds or 3.54 μradians or 0.52 core radii, where it has 45 % throughput. Of particular interest is the slope of throughput vs. image size. For the values given here that slope is

[2]Moffat $FWHM = 2R_{core}\sqrt{2^{1/\beta} - 1}$.

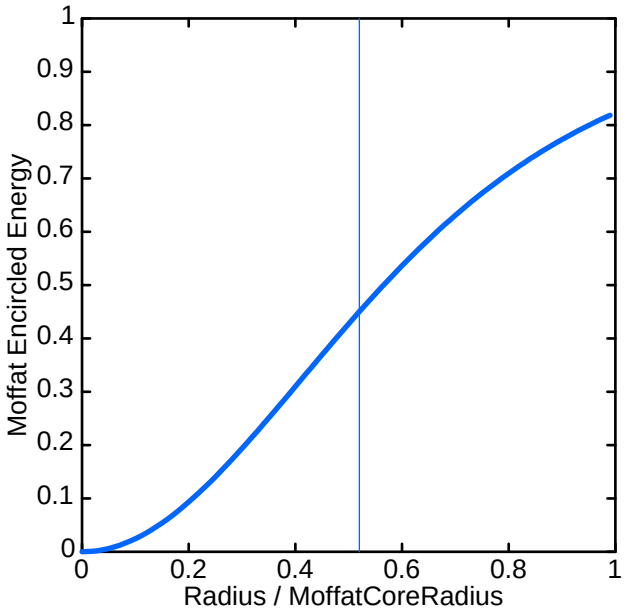

Figure 4: Throughput of a Moffat function. This curve is the basis of the throughput estimates in DocDB-347v3. A change in x by $\pm 1\%$ causes throughput change of $\pm 1.2\%$ in the vicinity of the half-throughput point. The vertical line represents a median DESI ELG viewed under median seeing conditions.

$dT_{relative}/d\theta_{relative} = -1.2$, that is to say that each percent growth in relative image size costs about 1.2 percent in relative throughput. We can use this rule to estimate the impact of the added MSF root-sum-square blur calculated in Figure 3 above:

$$\theta_{rms,total} = \sqrt{\theta^2_{rms,nominal} + \theta^2_{rms,added}} \tag{16}$$

Contrast a zero-slope-error corrector with the Figure 3 corrector whose $\theta_{rms,added} = 0.35\mu rad$. On top of a nominal $\theta_{rms,nominal} = 2.9\mu rad$, this Figure 3 corrector has $\theta_{rms,total} = 2.92\mu rad$, a growth of 0.67% and therefore a throughput hit of 0.8%. Of course the current throughput spreadsheet already includes the unknown mid-spatial contribution of the existing MOSAIC corrector/camera, so this change could work in either direction, but it does show that midspatials are a budget concern at the 1% throughput level.

6.2 Light Loss due to Scattering Beyond Fiber

At spatial frequencies somewhat above f_C, the PSD is likely to become steep with $p > 4$ which makes the HSF scattered light small. From equation 6 above, the loss fraction with a general power law index p becomes:

$$\eta_{loss} = \frac{8\pi^3 (N-1)^2\, A}{\lambda^2\, (p-2)} \cdot f_C^{2-p} \tag{17}$$

An example with $A = 10^{-15}$ and $p = 4$ is shown as the dotted red line in Figure 2 and as the final column in Figure 3. With these values the loss per surface is about 2×10^{-5} and twelve

corrector surfaces add up to 2.4×10^{-4}. Values this small are not significant in comparison with the other throughput factors, and need not be budgeted.

7 Fiber-View-Camera Position Errors

Just as the sky image is blurred passing through our corrector, so also the FVC fiber image centroids are perturbed, and these errors must be estimated and included in the fiber centroid position budget (which is another system throughput issue).

Low spatial frequencies do not contribute to the FVC position errors, because the fiducial interpolation process fits and removes low-frequency variations from the centroid maps. With 100 fiducials, only frequencies above about 4 cycles/diameter contribute, which is a low frequency cutoff of 5 cycles/m.

For any ray deviation pattern, the FVC pupil is the constraint (just as the telescope pupil is the constraint for galaxy viewing) and so the FVC ray variance on the focal plane is just the same as the galaxy ray variance. It may help to think of the FVC pupil as a projector delivering a spot to the focal plane using a very slow f/100 beam. Referred to sky angles, the angular contributions in Figure 3 apply to the FVC centroids as well as to the galaxy centroids. On the focal plane, 0.35 μrad corresponds to 5 μm of rms fiber position error, which will have to be budgeted alongside the other fiber centroid error contributors.

Studies of inhomogeneous refraction in large optical blanks (Schoenfeld et al 2005; Ladison and Maxon 2005) show that by far the largest variations across a blank have a magnitude of a few parts per million and are almost entirely at the lowest spatial frequencies, of the order of one cycle per blank diameter. When imaging, this variation reduces to a tilt and focus error that can be remedied through alignment and focussing, not through added blur. The FVC fiducial fits handle low frequencies completely. For this reason, inhomogeneities are unlikely to contribute significantly to the FVC position error budget.

8 Appendix: Distributions Used Here

Properties of Three Useful Distributions

	Gaussian	Moffat, $\beta = 3.5$	Sersic, $n = 1$
PSF	$exp(-r^2/2\sigma^2)$	$[1 + (r/r_c)^2]^{-\beta}$	$exp(-r/r_e)$
EE	$1 - exp(-r^2/2\sigma^2)$	$1 - [1 + (r/r_c)^2]^{1-\beta}$	$1 - (1 + r/r_e)exp(-r/r_e)$
$FWHM$	2.355 σ	0.936 r_c	1.386 r_e
$Ree50$	1.177 σ	0.565 r_c	1.678 r_e
r_{rms}	1.414 σ	0.8165 r_c	2.450 r_e

Here, the point spread function PSF is normalized to unity at r=0, and the encircled energy EE is normalized to unity for r=∞. FWHM is the diameter of the circle whose intensity is half the peak intensity. $Ree50$ is the radius of the circle that encircles half the total energy, and r_{rms} is the root mean square radius.

9 Appendix: Derivation of Equations 3 and 4

Consider an incident plane wave propagating in the $+z$ direction. Its complex field is

$$\psi(z) = exp(2\pi iz/\lambda) \tag{18}$$

Let this wave undergo a sinusoidal phase perturbation of amplitude a:

$$\phi(x) = a\ sin(2\pi fx) \tag{19}$$

The outgoing wave will have both z and x dependence, corresponding to multiple wave propagation into the x, z half space. If $f\lambda \ll 1$ the deviation angles will be small, and the net diffracted field will be closely approximated by

$$\psi(x, z) = exp[ia\ sin(2\pi fx) + 2\pi iz/\lambda] \tag{20}$$

The Jacobi-Anger expansion represents a phase modulated wave as a sum of pure waves:

$$exp[ia\ sin(2\pi fx)] = \sum_{n=-\infty}^{n=+\infty} J_n(a) \cdot exp(2\pi i\ nfx) \tag{21}$$

so the diffracted wave system can be written as a sum of plane waves:

$$\psi(x, z) = \sum_{n=-\infty}^{n=+\infty} J_n(a) \cdot exp[2\pi i\ (nfx + z/\lambda)] \tag{22}$$

Each plane wave therefore has a deviation angle of $\theta = \nabla x/\nabla z = nf\lambda$ and a wave amplitude of $J_n(a)$ or a power flux of $J_n^2(a)$. This scalar result appears to have been well known to Lord Rayleigh, who in 1907 worked out its closely-related vector form for polarized electromagnetic waves. However, near normal incidence, the scalar form will suffice.

For the simple sinusoidal phase shift pattern derived, here the positive and negative orders are sent to opposite sides of the zero order beam. To integrate diffracted power around a circularly symmetric pattern, both negative and positive orders contribute equal power, so the total $n-th$ order radial power is $2J_n^2(a)$.

Ground and polished surfaces will not be sinusoidal but will instead be composed of power in any spatial frequency band. These Fourier components are incoherent and their powers, not their amplitudes, combine giving $\phi_{rms} = a/\sqrt{2}$. We identify the unscattered power as the J_0^2 term, and the total integrated scatter as the remainder:

$$Unscattered = J_0^2(\sqrt{2}\phi_{rms}) = 1 - \phi_{rms}^2 \tag{23}$$

$$TIS = 1 - J_0^2(\sqrt{2}\phi_{rms}) = \phi_{rms}^2 \tag{24}$$

For a lens-air surface near normal incidence, $\phi_{rms} = 2\pi(N-1)\sigma/\lambda$ where the lens refractive index is N and the rms surface height distribution is σ. For a mirror, $\phi_{rms} = 4\pi\sigma/\lambda$.

10 Appendix: PSD integrals over $(0, \infty)$

All straight power laws diverge when integrated over $(0, \infty)$ but power laws with a break (a steepening of slope) can converge, and can therefore give finite result for diffracted power or angle over the entire range of spatial frequencies without an arbitrary division into spatial frequency regimes. This broken power law has four parameters: an overall coefficient, two power law exponents, and a crossover or break frequency f_{break} where these two power laws are equal:

$$PSD(f) = \frac{A}{f^a + f_{break}^{a-b} \cdot f^b} \tag{25}$$

The definite integral (Gradshteyn and Ryzhik 3.241 No.2)

$$\int_0^\infty \frac{x^m dx}{1+x^n} = \frac{\pi}{n\ sin[(m+1)\pi/n]} \tag{26}$$

exists when $0 < m{+}1 < n$. The first inequality gives convergence at $f = 0$ and the second gives convergence at $f = \infty$. From that we obtain

$$\int_0^\infty \frac{A\ f^c df}{f^a + f_{break}^{a-b} \cdot f^b} = \frac{\pi\ A\ f_{break}^{c-a+1}}{(b-a)\ sin[\pi(c-a+1)/(b-a)]} \tag{27}$$

provided that $a < c{+}1 < b$. In analogy with equation (1), setting $c = 1$ gives us the PSD integral for z_{rms}^2 and in analogy with equation (2), $c = 3$ gives us the PSD integral for s_{rms}^2.

Broken power laws have been employed by Harvey 1995, Toebben et al 1996, Walsh et al 1999, Cohen and Hull 2004, Sidick 2009, Hull et al 2012, and surely many others.

11 References

Aikens D.M., DeGroote J.E., and Youngworth R.N., "Specification and control of Mid-spatial frequency wavefront errors in optical systems," OSA OF+T (2008).

Alcock S.G., et al, "Using the PSD method to characterise the surface topography of optical surfaces," Proc SPIE 7801 (2010).

Church E. L., et al "Relationship between surface scattering and microtopographic features," Optical Engineering v.18 125-136 (1979).

Church E.L., "Fractal surface finish," Proc SPIE v 830 (1988).

Cohen E. and Hull A., "Selection of a mirror technology for the 1.8m Terrestrial Planet Finder demonstration mission," Proc SPIE v.5494 (2004).

Dey, A., and Valdes, F., "The delivered image quality with the MOSAIC Cameras at the Kitt Peak 4m and Cerro Tololo 4m Blanco Telescopes," PASP in press (2014).

Elson J.M. and Bennett, J.M., "Calculation of the PSD from surface profile data," Appl.Opt. 34 #1 201-208 (1995).

Gradshteyn I.S. and Ryzhik I.M. "Table of Integrals Series and Products," 2nd Edition, Academic Press (1980).

Harvey J.E., "Modeling the image quality of enhanced reflectance xray multilayers as a surface power spectral density filter function," Appl.Opt., v34 #19, pp.3715-3726 (1995).

Harvey, J.E., et al., "Nonparaxial scalar treatment of sinusoidal phase gratings," JOSA A 23, No4, 858-866 (2006).

Harvey J.E., et al., "Determining parametric Total Integrated Scatter behavior from optical fabrication metrology data," Proc SPIE 8126 (2011); also Opt.Eng. v.51 #1 (2012).

Harvey J.E., "Parametric analysis of the effect of scattered light upon the modulation transfer function," Opt. Eng. v.52 #7 (2013).

Hull, T., Riso,M., Barentine J.M., Magruder A., "Mid-spatial frequency matters," Proc SPIE 8353 (2012).

Jacoby, G.H., et al., "A new wide-field corrector for the Kitt Peak Mayall 4-m telescope," Proc. SPIE 3355 (1998).

Ladison J.L. and Maxon, J.E., "Improvement of homogeneity in large optics made of Corning HPFS fused silica," Proc SPIE v 5754 (2005).

Noll, R.J., "Effect of Mid- and High-Spatial Frequencies on optical performance," Opt.Eng., v.18 #2, pp.137-142 (1979).

Progler C. and Wong A., "Zernike coefficients: are they really enough?"; Proc SPIE 4000 pp.40-52, (2000)

Rayleigh, "On the dynamical theory of gratings," Proc. Roy. Soc., A 79, 399 (1907).

Rogers, J.R., "Slope error tolerances for optical surfaces," SPIE OptiFab Technical Digest TD04-04 (2007).

D. Schonfeld, T. Reuter, R. Takke, and S. Thomas, "Stitching oil-on interferometry of large fused silica blanks," Proc. SPIE 5965 (2005).

Sidick E., "Modelling PSD for Large Optics," Proc SPIE 7390 (2009).

Tamkin, J.H., and Milster, T.D., "Analysis and tolerancing of structured mid-spatial fre-

quency errors in imaging systems," Proc SPIE 7652 (2010).

Tamkin, J.H., Dallas, W.J., and Milster T.D., "Theory of point-spread function artifacts due to structured mid-spatial frequency surface errors," Appl. Opt. v.49 No 25 (2010).

Tobben H., et al., "The use of Power Spectral Density (PSD) to specify optical surfaces," Proc SPIE 2775 pp.240-250 (1996).

Youngworth R.N. and Stone B.D., "Simple Estimates of MSF," Appl.Opt. v 39 #13 2198 (2000).